Characterization of heat transfer in nanofluid spray cooling of a solid heated surface

Miguel Patrik Jyllilä Sanches

miguel.sanches@tecnico.ulisboa.pt

Instituto Superior Técnico, Universidade de Lisboa, Portugal

January 2021

Abstract

The interest in spray cooling has been increasing as an efficient thermal management technique for high power load systems such as electronics. The aim of this work was to study the use of nanofluids as a way of improving thermal performance of sprays. Nanofluids were prepared using as base solution distilled water with 0.05% (m/m) cetyltrimethylammonium bromide. Nanoparticles of alumina were mixed with the base fluid at different concentrations: 0.5%, 1% and 2% (m/m). Two different silver nanofluids were also prepared, using 1% (m/m) concentration, one using spherical and the other using triangular particles. These nanofluids were sprayed using a hollow-cone atomizer, at two different heights from an AISI 304 stainless steel foil. This foil was heated by Joule effect, with two imposed currents, delivering approximately 915 and 2100 W/m^2. Thermal footprints of the sprays were acquired using infrared thermography and dissipated heat fluxes were calculated. In steady-state, the lowest obtained temperatures at the surface occurred for the 0.5% (m/m) alumina nanofluid. Increasing alumina nanoparticle concentration resulted in the increase of radial foil temperatures. When comparing the silver nanofluids, the one with spherical particles resulted in slightly lower surface temperatures than the fluid with triangular particles. Heat transfer coefficients decreased with increasing thermal conductivity and dynamic viscosity of the nanofluids. On the other hand, it revealed a strong positive correlation with the specific heat capacity of the nanofluids. For the range of experimental conditions covered in this work, nanofluids have proven to increase the thermal performance of the spray.

Keywords: Spray cooling, Nanofluids, Heat transfer, Thermophysical properties, High-speed infrared thermography

1. Introduction

The increasing use of electronic systems and power electronics will require better and more efficient cooling mechanisms. The accumulation of heat leads to higher operating temperatures which have a negative impact on the lifetime and stability of equipment. One cooling technique with great potential to dissipate such high heat fluxes is spray cooling [1]. Spray cooling is a technique which is based on the impingement of small liquid droplets of a spray on a heated surface. This technique can be used in a single phase or two phase regime depending on the heat flux delivered by the surface and on the properties of the spray.

Apart from electronics cooling, other different applications have been identified for spray cooling, such as: dermatological operations and metal production and processing industry. In dermatological surgeries, cryogenic spray cooling is used to cool human skin before laser treatments. Spray cooling plays an important role in steel strip casting and optimizing the microstructure after hot rolling [2].

The heat transfer in spray cooling is a complex combination of different heat transfer mechanisms, [3, 4, 5]. This overall complex mechanism has not only to do with the heat transfer phenomena after droplet impact, but also has a strong relationship with the spray before impact [6]. Spray dynamics are dependent on atomizer type, injection pressure, type of fluid and even surrounding air velocities. These variables impact the atomization process, which is the progressive transformation of a continuous body of liquid into small droplets.

Moreover, heat transfer between the fluid and the surface is dependent on the impact of the fluid droplets. Different studies have been performed to understand the possible outcomes of a droplet impact on to solid surface, [7, 8, 6, 9]. However, these studies focus mainly on individual droplet collision with the solid body, as the study of single droplets in a spray is a big experimental challenge. As explained by Moreira [6], the extrapolation of

1

these results for individual droplet impact outcomes to sprays must be made carefully, as the droplet-droplet interactions are neglected.

The need for better cooling systems has not only resulted in the design of new cooling methods, but the use of different and more sophisticated cooling fluids has also been explored. In fact, cooling performance depends on the overall system, which includes the cooling fluid. Given the abundance and cost of water and air, they are by far the most used cooling agents. Nevertheless, other refrigeration fluids are also found in some applications. In some cases, the specific heat performance of these fluids may not be enough, thus emerged the idea of combining the properties of a base fluid and solid particles.

Nanofluids are suspensions of nanoparticles in a base fluid. These nanoparticles are typically in the range of $10 - 100$ nm and are usually metallic. However, different materials may be found depending on the specific application, such as: ceramics, metallic oxides or carbonic. The term nanofluids was introduced by Choi and Eastman [10]. Yet, the idea of scattering solid particles into liquids is not new, and may be related to as early as 1873 with the work of Maxwell [11]. Maxwell explored the properties of a fluid with micrometre and millimetre level particles. However, this scale particles have limited application in heat transfer enhancement, due to settling, abrasion and clogging [12].

Heat transfer enhancement by the use of nanofluids is an ongoing research field. The mechanisms behind heat transfer in nanofluids are very complex, resulting of liquid-particle and particle-particle interactions. Nanofluids show significant enhancement of thermal conductivity when compared to the base fluid. This has not only to do with the higher thermal conductivity of the solid particles but also with the high specific surface area of the nanoparticles [13].

In this work, both these high-tech engineering solutions were combined. Sprays of different nanofluids were compared with water to study the differences on the cooling of a solid heated surface.

2. Implementation
2.1. Fluids preparation and characterization
For this work nanofluids of alumina (Al_2O_3) and silver (Ag) were prepared in a distilled water and 0.05% (m/m) cetyltrimethylammonium bromide (CTAB) base fluid. Alumina nanofluids were prepared in three different mass concentrations: 0.5%, 1% and 2% (m/m), using a two-step preparation method [14]. Alumina nanoparticles were acquired from Alfa Aesar and had particle sizes between 40 and 50 nm. On the other hand, two 1% (m/m) silver nanofluids were prepared using an one-step preparation method [15, 16], one with spherical and the other with triangular shaped nanoparticles.

The base fluid and nanofluids were characterized in terms of thermal conductivity [13, 17], specific mass and specific heat capacity [18], using theoretical models. Moreover, surface tension and wettability, quantified by the static contact angle with the test surface, were determined experimentally using a *THETA* optical tensiometer by *Attension*.

Table 1 summarizes the calculated properties of the fluids, specific mass ρ, specific heat capacity c_p and thermal conductivity k.

Fluid	ρ [g/cm^3]	c_p [kJ/(kg.K)]	k [W/(mK)]
Water	0.9982	4.22	0.6060
Base fluid	0.9987	*	*
0.5% (m/m) Al$_2$O$_3$	1.0024	4.20	0.6082
1.0% (m/m) Al$_2$O$_3$	1.0062	4.19	0.6104
2.0% (m/m) Al$_2$O$_3$	1.0108	4.15	0.6149
1.0% (m/m) Ag spher.	1.0229	4.12	0.6106
1.0% (m/m) Ag trian.	1.0229	4.12	0.6096

Table 1: Calculated fluid properties at 25 °C. ρ is specific mass, c_p is specific mass capacity and k is thermal conductivity. (* – c_p and k of CTAB were not found in literature, thus these properties of the base fluid are considered equal to those of water, which is a good approximation given the low CTAB concentration used).

As seen in Table 1, ρ and k increase with the addition of the nanoparticles. On the other hand, c_p decreases with increasing amount of nanoparticles. Moreover, for the same mass concentration of nanoparticles, 1.0% (m/m) alumina (Al_2O_3) nanofluid shows higher c_p than silver nanofluids. However, given the higher thermal conductivity of silver and thermal conductivity dependence on nanoparticle shape [13], silver nanofluid with spherical particles has higher thermal conductivity, followed by triangular silver nanofluid and finally by the 1.0% (m/m) alumina nanofluid.

Properties of CTAB were not found in literature. For this reason, the properties of the base fluid (distilled water with 0.05% (m/m) CTAB) were considered equal to those of water, except for the surface tension, as aforementioned. This is a good approximation for most of the properties, given the low concentration of CTAB used. However, literature shows that surfactants tend to deteriorate the thermal performance of fluids [19].

Table 2 summarizes the experimentally determined properties of the fluids: dynamic viscosity μ, surface tension σ and static contact angle with the test surface θ. The surface tension and static contact angles were measured at temperature 24 °C and are presented as the mean and standard deviation of 15 and 5 consecutive measures, respectively. Dynamic viscosity was measured using a *TA in-*

struments *ARI 500 ex* rheometer, at temperature 20 °C, with an accuracy of ±5%.

Fluid	μ [mPa.s]	σ [mN/m]	θ [°]
Water	1.009	74.60 ± 2.22	86.47 ± 6.41
Base fluid	1.291	35.92 ± 0.92	53.58 ± 6.33
0.5% (m/m) Al_2O_3	3.572	39.03 ± 1.27	61.80 ± 2.88
1.0% (m/m) Al_2O_3	6.815	40.18 ± 2.70	59.89 ± 2.70
2.0% (m/m) Al_2O_3	8.835	40.24 ± 0.86	57.89 ± 11.28
1.0% (m/m) Ag spher.	13.175	40.01 ± 0.42	51.09 ± 3.45
1.0% (m/m) Ag trian.	18.903	43.07 ± 0.36	47.32 ± 6.30

Table 2: Experimentally determined fluid properties and contact angle with test surface. μ is dynamic viscosity, σ is surface tension and θ is contact angle with the test surface.

As seen in Table 2, with the addition of the sufactant, σ and θ decrease to half the values for distilled water. Moreover, increasing the nanoparticle concentration results in an increase of σ and slight decrease in θ. For the same mass concentration, 1.0% (m/m) alumina nanofluid has the highest θ, followed by spherical silver and then triangular silver nanofluids. On the other hand, still for the same mass concentration of 1% (m/m), triangular silver nanofluid has the highest surface tension, followed by alumina and then spherical silver nanofluids.

2.2. Experimental setup

The fluids were sprayed using a hollow-cone pressure-swirl atomizer, placed at two different heights from a thin AISI 304 stainless steel foil. The foil has a width of 60 mm, length of 90 mm and thickness of 20 μm. This foil was proven to be smooth using a profilometer with 20 nm resolution [20, 21].

The foil was heated by Joule effect q''_{Joule}, Equation 1, with two different applied currents I. One for $I = 10$ A which resulted in an input heat flux of approximately $q''_{\text{Joule}} \approx 914.50$ W/m^2 and an initial surface temperature of $T_0 \approx 84.14$ °C, and $I = 15$ A which resulted in an input heat flux of approximately $q''_{\text{Joule}} \approx 2104.98$ W/m^2 and an initial surface temperature of $T_0 \approx 140.97$ °C.

$$q''_{\text{Joule}} = R \times I^2 \qquad (1)$$

Where R is the electrical resistance of the foil.

This foil was fixed horizontally on a support which was then placed over a *Xenics' Onca-MWIR-InSb-320* high-speed infrared thermography camera to record the thermal footprints of the sprays, as illustrated in Figure 1. A *Vision Research Phantom v4.2* high-speed camera was placed laterally to the spray. The fluids were placed inside a 3 L vessel pressurized at 0.5 MPa, which fed the atomizer at a mass flow rate of approximately 7 kg/h.
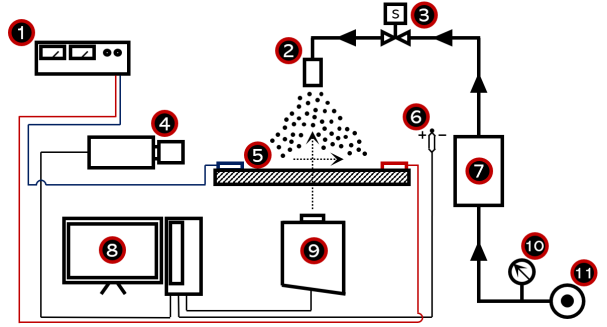

Figure 1: Experimental setup. (1) Power supply, (2) Pressure-swirl atomizer, (3) Normally-closed solenoid valve, (4) High-speed camera, (5) AISI 304 Stainless Steel foil, (6) Thermocouple, (7) 3 L pressurized vessel, (8) Data acquisition computer, (9) Thermographic camera, (10) Pressure gauge, (11) Pressurized air source.

The acquired thermal footprints of the sprays impacting on the stainless steel foil were then processed using an adapted version of the thermographic camera video processing MATLAB code developed by Pontes [21]. The high-level algorithm of this routine is presented in Figure 2.
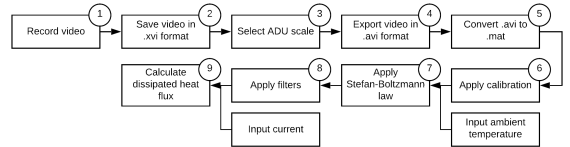

Figure 2: Thermographic video processing algorithm.

The thermographic camera captures the energy emitted by the object and transforms it to a value of Analog to Digital Unit (ADU). The role of the processing code starts at point (5) of Figure 2. Then the ADU values are converted back to energy intensities by applying the calibration (6). The ambient temperature is input to the program to subtract the contribution of atmosphere radiation. Thereafter, Stefan-Boltzmann law is applied to obtain object temperature (7). Finally, a weighted background removal filter [21] and a Gaussian filter with standard deviation 2 and a 9×9 pixel kernel are applied.

A Biot number Bi, Equation 2, analysis was performed to analyse the assumption of constant temperature across the foil, which is valid for $Bi << 1$ [22].

$$Bi = \frac{h_c \times \delta}{k_h} \qquad (2)$$

In the present case, $\delta = O(10^{-5})$m, $k_h = O(10^1)$W/(m.K) and $h_c = O(10^3)$W/(m^2.K), thus

3

from Equation 2, $Bi = O(10^{-3}) << 1$. The condition is met, thus the approximation is valid.

The thermographic videos are then used to calculate the dissipated heat flux from the foil. This is performed by performing pixel energy balances, Figure 3.
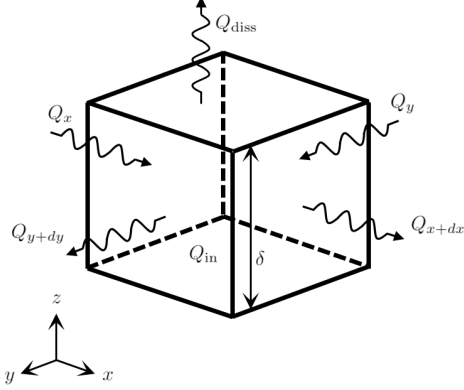

Figure 3: Pixel energy exchanges.

Where δ is the foil thickness, $(Q_{x+dx} - Q_x)$ is the heat transferred to the neighbouring pixels in the x direction, $(Q_{y+dy} - Q_y)$ is the heat transferred to the neighbouring pixels in the y direction, Q_{in} is the heat generated by Joule effect and Q_{diss} is the heat dissipated through the top and bottom surfaces.

The energy balance to the pixel is mathematically written as:

$$q''_{diss} = q''_{in} + k_h \delta \left(\frac{\partial^2 T}{\partial x^2} + \frac{\partial^2 T}{\partial y^2} \right) - \rho_h c_{p,h} \delta \frac{\partial T}{\partial t} \quad (3)$$

Where q'' are heat fluxes, k_h is the thermal conductivity of the foil, ρ_h is the density of the foil, $c_{p,h}$ is the specific heat capacity of the foil, $\frac{\partial^2 T}{\partial x^2}$ and $\frac{\partial^2 T}{\partial y^2}$ are the second order partial derivatives of temperature T with respect to x and y directions, respectively, and $\frac{\partial T}{\partial t}$ is the partial derivative of T with respect to time t. q''_{in} is calculated from Equation 1.

In this work, density ρ_h and specific heat capacity $c_{p,h}$ of the stainless steel foil are assumed to be constant with temperature, $\rho_h = 7880$ kg/m^3 and $c_{p,h} = 477$ J/(kg.K).

Due to the strong dependence of electrical resistance R and thermal conductivity k_h of the foil with temperature, these properties were obtained, for each temperature, from linear fittings of data. For the electrical resistance R, the voltage was measured for different input currents and then the resistance calculated. The following interpolation was obtained for R (in Ω and T in °C), with coefficient of determination equal to 0.9822.

$$R = 2 \times 10^{-5} \times T + 0.0477 \quad (4)$$

For the thermal conductivity k, the data from Ho and Chu [23] was used to build the following interpolation (with k in W/(m.K) and T in °C), with coefficient of determination equal to 0.9996.

$$k_h = 0.0171 \times T + 14.425 \quad (5)$$

Previous studies of this specific spray atomizer [20, 24] had already shown no significant variations in atomization for the different nanofluids.

The various fluids were compared in terms of dissipated heat flux as they impact on the surface q''_{diss}, surface temperatures T and thermal performance evaluated as heat transfer coefficient h, which is given by:

$$h = \frac{q''_{diss}}{\Delta T} \quad (6)$$

Where $\Delta T = T_w - T_f$. T_f is the fluid temperature.

2.3. Experimental procedure

After measuring the temperature of the fluid to be tested, the fluid is placed inside the high pressure vessel. The nozzle height relative to the foil is adjusted as necessary. Then, the compressed air valve is open to pressurize the vessel. A thermographic video with 5 frames of the foil before heating is recorded. Thereafter, the power source is turned on and set to the desired current. While the foil temperature increases, the ambient temperature and the difference of electric potential between the contacts are checked using the multimeter and registered. Once the temperature of the foil has stabilized, the thermographic and high-speed recordings are initiated. The solenoid valve is only opened once the thermographic camera recording rate has stabilized. When the recordings have finished, the surface is cleaned using acetone and distilled water. For each experimental condition, three identical tests were performed in a row. When changing the test fluid, all wet parts are cleaned with distilled water and dried.

3. Results and discussion

As explained in Section 3 (Implementation), two input currents I were selected $I = 10$ A and $I = 15$ A. Moreover, the atomizer was placed at two different heights from the metallic foil Z: $Z = 10$ mm and $Z = 20$ mm. Combined, resulted in the study of four working conditions.

In this Section the results are presented and discussed. First the water spray is analysed in the different working conditions. Thereafter, the base fluid spray is analyzed to isolate the effect of adding the surfactant CTAB. Then different concentrations of alumina nanoparticles are compared, followed by the study of nanofluids prepared with silver nanoparticles of different shapes. Finally, an overall comparison is performed and nanofluid properties

are related with the thermal performance of the resulting spray upon its impact on the heated surface.

The temperature of each fluid was measured before each experiment and was seen to be equal to $T_f = 21.82 \pm 0.03\ °C$.

3.1. Water spray

Figures 4 and 5 show the time evolution of the foil temperature relative to the fluid temperature ΔT, for distilled water sprays and working conditions with $I = 10$ A and $I = 15$ A respectively.
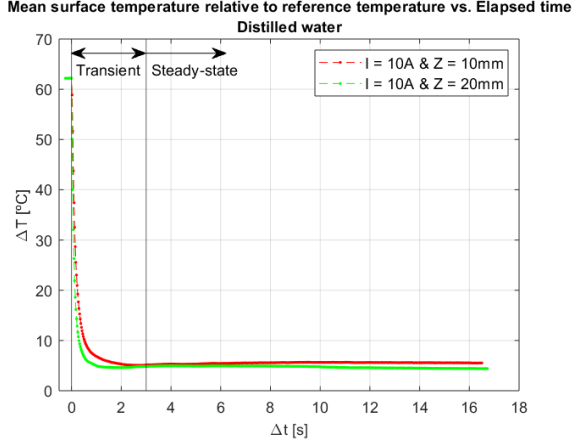

Figure 4: Foil temperature relative to fluid reference temperature ΔT for water spray and $I = 10$ A conditions as a function of time since first fluid contacts with surface.
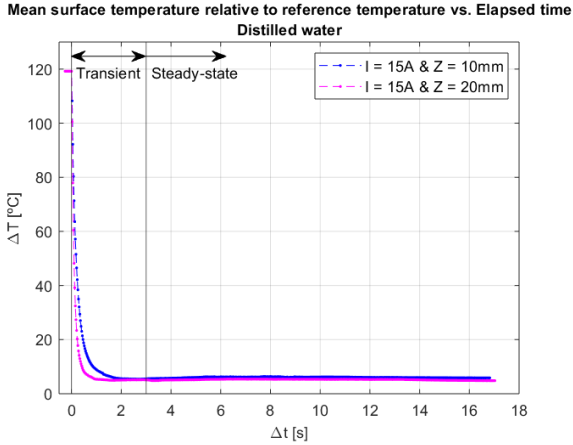

Figure 5: Foil temperature relative to fluid reference temperature ΔT for water spray and $I = 15$ A conditions as a function of time since first fluid contacts with surface.

Figures 4 and 5 show two regimes for $\Delta t > 0$ s. One is the transient regime were the temperature drastically decreases from the initial foil temperature to close to the fluid temperature. This regime is followed by a steady-state regime were temperatures no longer change with time.

Comparing the curves for $Z = 10$ mm and $Z = 20$ mm show that for the $Z = 20$ mm conditions the temperature decreases and stabilizes slightly faster than for $Z = 10$ mm conditions. This has to do with the fact that, by placing the atomizer higher relative to the foil, the spray footprint is larger, thus covering a larger area of the foil, resulting in faster cooling.

Figures 6 and 7 show the time evolution of the dissipated heat flux q''_{diss}, for distilled water sprays and working conditions with $I = 10$ A and $I = 15$ A respectively.
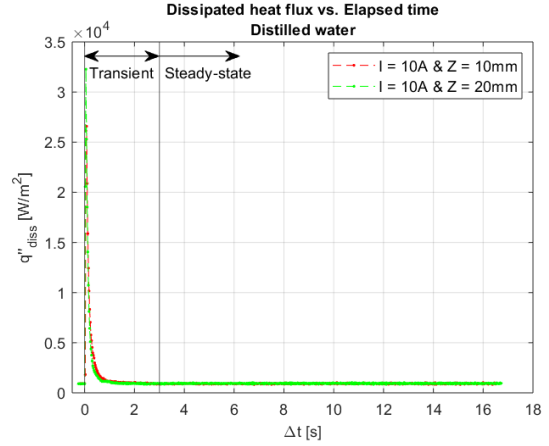

Figure 6: Dissipated heat flux q''_{diss} for water spray and $I = 10$ A conditions as a function of time since first fluid contacts with surface.
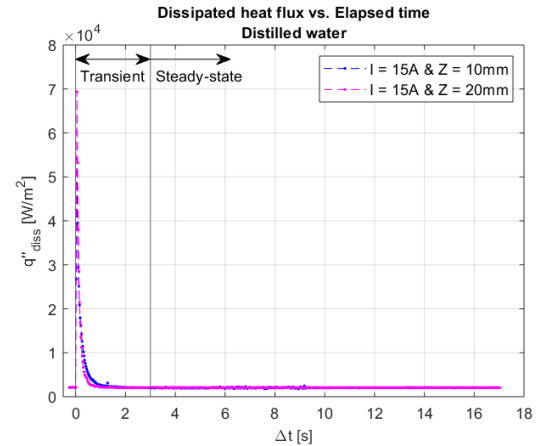

Figure 7: Dissipated heat flux q''_{diss} for water spray and $I = 15$ A conditions as a function of time since first fluid contacts with surface.

Similarly to what was seen for ΔT, the dissipated heat flux q''_{diss} plots presented in Figures 6 and 7 also show two different regimes for $\Delta t > 0$ s. In this case the transient regime is characterized by a spike in

the dissipated heat flux, which then decreases. This regime is followed by the steady-state regime where again no variations in the dissipated heat flux are verified.

The maximum dissipated heat flux is higher for the $Z = 20$ mm conditions when compared to the $Z = 10$ mm conditions. This is a result of the sharper decrease in temperatures verified in Figures 4 and 5 for the $Z = 20$ mm conditions.

Table 3 are the dissipated heat flux q''_{diss}, mean foil temperature relative to fluid temperature $\overline{\Delta T}$ and heat transfer coefficient h in steady-state for water sprays in the different working conditions. The results are presented as mean values and standard deviations for three consecutive equal measures. Heat transfer coefficients h are calculated using Equation 6.

I [A]	Z [mm]	q''_{diss} [W/m^2]	$\overline{\Delta T}$ [°C]	h [W/(m^2.°C)]
10	10	895.71 ± 6.16	26.19 ± 0.03	34.20 ± 0.24
	20	903.98 ± 3.18	24.98 ± 0.01	36.18 ± 0.13
15	10	2010.14 ± 7.89	27.86 ± 0.05	72.14 ± 0.31
	20	2024.10 ± 6.33	27.29 ± 0.05	74.16 ± 0.27

Table 3: Steady-state dissipated heat flux q''_{diss}, mean foil temperature relative to fluid temperature $\overline{\Delta T}$ and heat transfer coefficient h for water sprays in the different working conditions.

Table 3 shows that the highest heat transfer coefficients are obtained for $Z = 20$ mm conditions.

Due to some oscillations in the recording rate of the thermographic camera, only the steady-state will be compared between the different fluids.

3.2. Effect of the surfactant

Figure 8 shows the radial foil temperature profile relative to fluid temperature ΔT for distilled water and base fluid (distilled water with 0.05% (m/m) cetyltrimethylammonium bromide or CTAB) sprays when $I = 15$ A and $Z = 10$ mm.
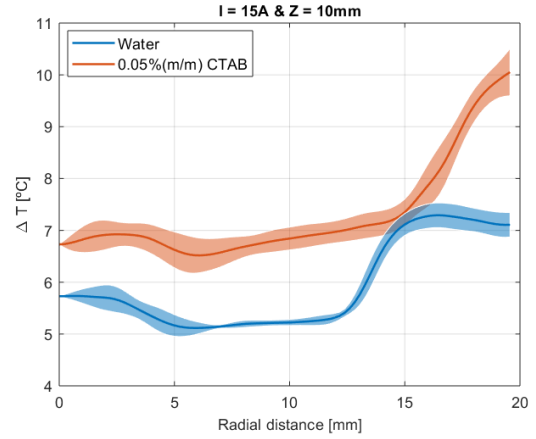

Figure 8: Radial foil temperature profile relative to fluid temperature ΔT for distilled water and base fluid sprays when $I = 15$ A and $Z = 10$ mm.

For all working conditions, the radial foil temperature profiles for the base fluid sprays were higher than those of distilled water sprays. This agrees with studies reported in the literature, e.g. [19], who report a deterioration of the thermal performance with the addition of surfactant.

Moreover, as suggested by Figure 8, the shape of the profile changed. With the surfactant, the curves became more flat. This is related with the increased wettability of the base fluid when compared to water, as seen in Table 2, given by the lower contact angle.

Table 4 shows the steady-state dissipated heat flux q''_{diss}, mean foil temperature relative to fluid temperature $\overline{\Delta T}$ and heat transfer coefficient h for the base fluid sprays in the different working conditions.

I [A]	Z [mm]	q''_{diss} [W/m^2]	$\overline{\Delta T}$ [°C]	h [W/(m^2.°C)]
10	10	909.23 ± 3.35	27.08 ± 0.03	33.50 ± 0.13
	20	906.71 ± 5.33	25.69 ± 0.01	35.28 ± 0.21
15	10	2038.00 ± 7.16	29.77 ± 0.08	68.50 ± 0.30
	20	2034.33 ± 8.73	26.67 ± 0.03	76.16 ± 0.34

Table 4: Steady-state dissipated heat flux q''_{diss}, mean foil temperature relative to fluid temperature $\overline{\Delta T}$ and heat transfer coefficient h for base fluid sprays in the different working conditions.

Comparing the steady-state values for water and the base fluid, Tables 3 and 4 respectively, for all working conditions, the dissipated heat flux increased with the addition of the surfactant. On the other hand, the mean surface temperatures increased, thus resulting in lower heat transfer coefficients for the base fluid.

3.3. Alumina nanofluids

Alumina nanofluid sprays were studied in different mass concentrations: 0.5, 1.0 and 2.0% (m/m). Fig-

ure 9 shows the radial foil temperature profile relative to fluid temperature ΔT for alumina nanofluids and base fluid sprays when $I = 15$ A and $Z = 10$ mm.

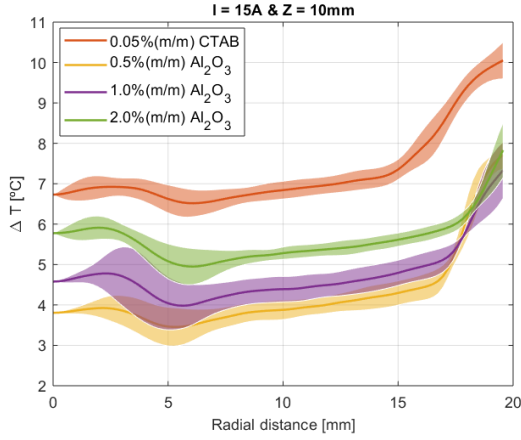Figure 9: Radial foil temperature profile relative to fluid temperature ΔT for alumina nanofluids and base fluid sprays when $I = 15$ A and $Z = 10$ mm.

For all working conditions, when adding alumina nanoparticles the shape of the radial temperature profiles is not significantly affected when compared to the base fluid. However, the increase of alumina nanoparticle concentration results in the displacement of the temperature profiles to higher temperatures. In fact, the lowest foil temperatures were obtained for the 0.5% (m/m) concentration nanofluid.

Table 5 shows the steady-state dissipated heat flux q''_{diss}, mean foil temperature relative to fluid temperature $\overline{\Delta T}$ and heat transfer coefficient h for the alumina nanofluids sprays in the different working conditions.

I [A]	Z [mm]	Alumina content [%(m/m)]	q''_{diss} [W/m²]	$\overline{\Delta T}$ [°C]	h [W/(m².°C)]
10	10	0.5	907.16 ± 3.50	24.23 ± 0.01	37.45 ± 0.15
		1	909.25 ± 3.95	25.83 ± 0.01	35.20 ± 0.15
		2	910.82 ± 3.80	26.75 ± 0.02	34.05 ± 0.14
	20	0.5	902.81 ± 3.95	23.81 ± 0.01	37.92 ± 0.17
		1	903.57 ± 4.09	24.44 ± 0.01	36.96 ± 0.17
		2	902.87 ± 4.02	25.56 ± 0.01	35.33 ± 0.16
15	10	0.5	2046.67 ± 7.04	26.57 ± 0.04	77.40 ± 0.29
		1	2042.88 ± 5.96	27.31 ± 0.03	74.81 ± 0.23
		2	2042.11 ± 7.84	27.65 ± 0.02	73.87 ± 0.29
	20	0.5	2019.65 ± 4.48	24.99 ± 0.01	80.81 ± 0.18
		1	2025.39 ± 4.55	25.40 ± 0.01	79.75 ± 0.18
		2	2022.01 ± 4.65	26.62 ± 0.01	75.95 ± 0.18

Table 5: Steady-state dissipated heat flux q''_{diss}, mean foil temperature relative to fluid temperature $\overline{\Delta T}$ and heat transfer coefficient h for alumina nanofluids sprays in the different working conditions.

In accordance with what was seen for the radial foil temperature profiles, Table 5 shows a decrease in heat transfer coefficients h for increasing alumina nanoparticle content. This may be a result of increased viscosity, which deteriorates fluid motion,

and decreased specific heat capacities, thus compromising heat transfer by convection.

3.4. Silver nanofluids

To study the impact of nanoparticle shapes, two shapes of silver nanoparticles were used to prepare two different nanofluids at the same mass concentration of 1% (m/m). One with spherical nanoparticles and the other with triangular.

Comparing the radial foil temperature profiles for these two nanofluids to the ones of the base fluid resulted in slightly lower temperatures with the addition of silver nanoparticles. However, for the experimental conditions of this work, no significant changes were observed between the two silver nanofluids.

Table 6 shows the steady-state dissipated heat flux q''_{diss}, mean foil temperature relative to fluid temperature $\overline{\Delta T}$ and heat transfer coefficient h for the silver nanofluids sprays in the different working conditions.

I [A]	Z [mm]	Nanoparticle shape	q''_{diss} [W/m²]	$\overline{\Delta T}$ [°C]	h [W/(m².°C)]
10	10	Spherical	909.05 ± 5.75	26.16 ± 0.02	34.75 ± 0.22
		Triangular	910.11 ± 4.55	27.26 ± 0.02	33.39 ± 0.17
	20	Spherical	907.55 ± 3.18	25.38 ± 0.02	35.75 ± 0.13
		Triangular	907.58 ± 5.54	25.71 ± 0.01	35.31 ± 0.22
15	10	Spherical	2035.34 ± 7.23	27.99 ± 0.07	72.72 ± 0.32
		Triangular	2037.43 ± 7.91	28.99 ± 0.07	70.28 ± 0.32
	20	Spherical	2029.24 ± 6.62	26.57 ± 0.04	76.36 ± 0.27
		Triangular	2026.31 ± 4.61	26.55 ± 0.01	76.31 ± 0.18

Table 6: Steady-state dissipated heat flux q''_{diss}, mean foil temperature relative to fluid temperature $\overline{\Delta T}$ and heat transfer coefficient h for silver nanofluids sprays in the different working conditions.

Comparing the results for the base fluid, Table 4, and for the silver nanofluids, Table 6, show negligible differences between them in terms of heat transfer coefficients.

3.5. Overall comparison

Figures 10, 11 and 12 are the heat transfer coefficients h for the different nanofluids as a function of their thermal conductivity k, specific heat capacity c_p and dynamic viscosity μ, respectively.
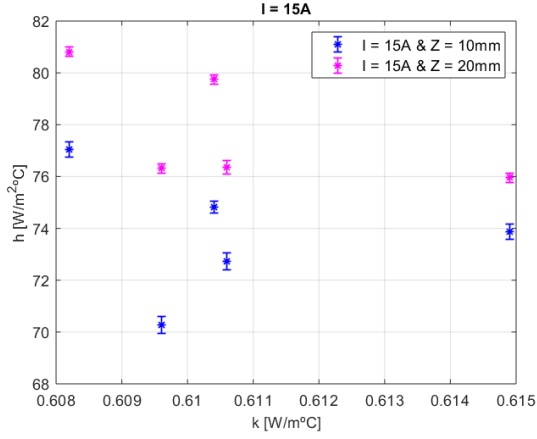
Figure 10: Heat transfer coefficient h as a function of the thermal conductivity k for the different nanofluids in $I = 15$ A conditions.
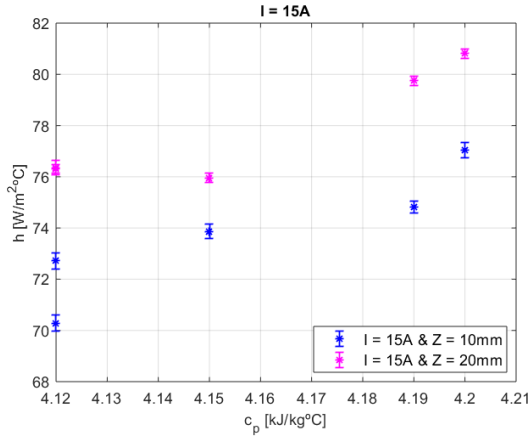

Figure 11: Heat transfer coefficient h as a function of the specific heat capacity c_p for the different nanofluids in $I = 15$ A conditions.
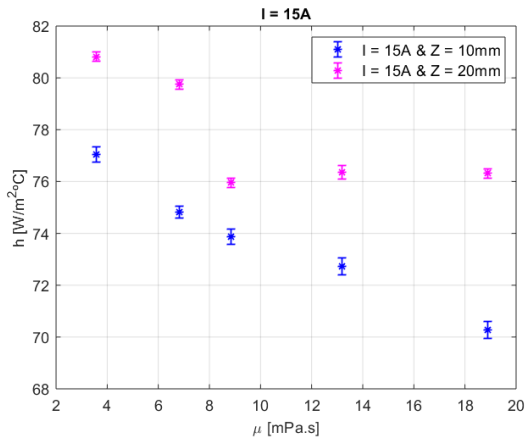

Figure 12: Heat transfer coefficient h as a function of the dynamic viscosity μ for the different nanofluids in $I = 15$ A conditions.

Figure 10 shows a slight decrease of heat transfer coefficient h with increasing thermal conductivity of the nanofluids k. This reduction in thermal performance may be associated with the experimental conditions used in this work, thus other properties of the fluid prevail over the increase in thermal conductivity.

On the contrary, increasing the specific heat capacity of the fluid c_p resulted in an increase of heat transfer coefficients h, Figure 11. This agrees with the definition of heat transfer coefficient and dissipated heat flux by convection, as they are proportionally related to each other by the mass of fluid.

Figure 12 shows the negative impact of the increase in dynamic viscosity in the thermal performance of the fluids. The increase in viscosity not only deteriorates heat transfer by convection, but also hampers fluid flow on the surface.

3.6. Nanofluid stability

Nanofluid stability is very important to practical applications of this type of fluids. The particles interact with each other and with the base fluid, which can have a positive or negative impact on the overall stability and thermal performance of the fluids. A visual long-term periodic analysis of the fluids was performed to study their stability.

Once prepared, the silver nanoparticles started to oxidize immediately. This deterioration is faster when the fluid is subject to higher temperatures and incident light. On the other hand, alumina nanoparticles are chemically stable. Only some precipitate could be seen after 48 hours at rest. However, with some minutes in the ultrasonicator, the homogeneity of the alumina nanofluids would be restored.

4. Conclusions

This paper compares the thermal performance of different nanofluid sprays. Nanofluids of different concentrations of alumina and nanofluids of silver with different particle shapes were compared to distilled water spray and to the base fluid used to prepare the nanofluids (distilled water with 0.05% (m/m) CTAB). Thermal performance of the sprays was compared using the heat transfer coefficient h, i.e. higher h correspond to higher thermal performance.

Higher height of the atomizer relative to the heated surface resulted in higher thermal performances. This was seen to be a result of the higher level of atomization and larger footprint of the spray when the spray is placed higher. Moreover, when the atomizer is placed closer to the surface, the speeds of the droplets are higher, which promotes splashing and rebound of the droplets from the liquid film [20, 24].

Overall, from the studied fluids, the alumina

nanofluid with lowest mass concentration resulted in the highest heat transfer coefficients. In fact, for the 0.5% (m/m) alumina nanofluid the heat transfer coefficients were higher than for distilled water in all working conditions. Increasing the concentration of alumina nanoparticles resulted in worse thermal performance. Increasing specific heat capacities were associated with higher heat transfer coefficients. In contrast to literature, for the experimental conditions of this work, increasing thermal conductivity resulted in slightly smaller heat transfer coefficients. Similarly, increasing dynamic viscosity of the fluids was also seen to have a negative impact on the thermal performance of the sprays, as it affects fluid flow, deteriorating heat transfer by convection. No significant changes were observed for the silver nanofluids of different particle shapes.

Visual inspection of the stability of the silver nanofluids showed a high compromise of the stability for this type of nanofluids due to oxidation. On the other hand, alumina nanofluids revealed long time stability, of approximately 48 hours, and ultrasonication for some minutes would restore homogeneity.

This study shows that nanofluids are capable of enhancing thermal performance of sprays. However, due to increased dynamic viscosity of the fluids with higher nanoparticle concentrations, this enhancement disagrees with the increase in thermal conductivity. In fact, the dominating heat transfer mechanism for the conditions of this work was seen to be convection. Further studies need to be developed with the objective of optimizing the thermophysical properties of the nanofluids, which should be specific for each working condition.

References

[1] B. S. Glassman. Spray cooling for land, sea, air and space based applications, a fluid management system for multiple nozzle spray cooling and a guide to high heat flux heater design. Master's thesis, Department of Mechanical, Materials and Aerospace Engineering, University of Central Florida, 2005.

[2] Z. Yan. Spray cooling. *Two Phase Flow, Phase Change and Numerical Modeling*, 13:285–310, 2011.

[3] M. R. Pais, L. C. Chow, and E. T. Mahefkey. Surface roughness and its effect on the heat transfer mechanism in spray cooling. *Journal of Heat Transfer*, 114:211–219, 1992.

[4] J. Yang, L. C. Chow, and M. R. Pais. Nucleate boiling heat transfer in spray cooling. *Journal of Heat Transfer*, 188:668–671, 1996.

[5] D. P. Rini, R. H. Chen, and L. C. Chow. Bubble behaviour and nucleate boiling heat transfer in saturated FC-72 spray cooling. *Journal of Heat Transfer*, 124:63–72, 2002.

[6] A. L. N. Moreira, A. S. Moita, and M. R. Panão. Advances and challenges in explaining fuel spray impingement: How much of a single droplet impact research is useful. *Progress in Energy and Combustion Science*, 36:554–580, 2010.

[7] A. S. Moita and A. L. N. Moreira. Drop impact onto cold and heated rigid surfaces: morphological comparisons, disintegration limits and secondary atomization. *International Journal of Heat and Fluid Flow*, 28(4):735–772, 2007.

[8] A. Moita. *Thermal and Fluid Dynamics of Droplet Wall Interaction*. PhD thesis, Department of Mechanical Engineering, Instituto Superior Técnico, Lisbon, 2009.

[9] C. Mundo, M. Sommerfeld, and C. Tropea. Droplet-wall collisions: experimental studies of the deformation and breakup process. *International Journal Multiphase flow*, 21(2):151–173, 1995.

[10] Stephen US Choi and Jeffrey A Eastman. Enhancing thermal conductivity of fluids with nanoparticles. Technical report, Argonne National Lab., IL (United States), 1995.

[11] J. C. Maxwell. *A Treatise on Electricity and Magnetism*. 1873.

[12] Y. Xuan and Q. Li. Heat transfer enhancement of nanofluids. *International Journal of Heat and Fluid Flow*, 21:58–64, 2000.

[13] H. S. Aybar, M. Sharifpur, M. R. Azizian, M. Mehrabi, and J. P. Meyer. A review of thermal conductivity models for nanofluids. *Heat Transfer Engineering*, 2015.

[14] Babita, S. K. Sharma, and S. M. Gupta. Preparation and evaluation of stable nanofluids for heat transfer application: A review. *Experimental Thermal and Fluid Science*, 79:202–212, 2016.

[15] J. S. Suh, D. P. DiLella, and M. Moskovits. Surface-enhanced raman spectroscopy of colloidal metal systems: a two-dimensional phase equilibrium in p-aminobenzoic acid adsorbed on silver. *Journal of Physical Chemistry*, 87:1540–1544, 1983.

[16] J. A. Creighton, C. G. Blatchford, and M. G. Albrecht. Plasma resonance enhancement of

Raman scattering by pyridine adsorbed on silver or gold sol particles of size comparable to the excitation wavelength. *Journal of the Chemical Society Faraday Transactions II*, 75:790–798, 1979.

[17] R. L. Hamilton and O. K. Crosser. Thermal conductivity of heterogeneous two-component systems. *Industrial Engineering Chemistry Fundamentals*, 1:182–191, 1962.

[18] K. V. Sharma, P. K. Sarma, W. H. Azmi, R. Mamat, and K. Kadirgama. Correlations to predict friction and forced convection heat transfer coefficients of water based nanofluids for turbulent flow in a tube. *The International Journal of Microscale and Nanoscale Thermal and Fluid Transport*, 3(4), 2012.

[19] A. H. A. Al-Waeli, M. T. Chaichan, H. A. Kazem, and K. Sopian. Evaluation and analysis of nanofluid and surfactant impact on photovoltaic-thermal systems. *Case Studies in Thermal Engineering*, 13, 2019.

[20] M. Figueiredo. Nanofluid spray cooling characterization combining phase doppler anemometry with high-speed visualization and thermography. Master's thesis, Instituto Superior Técnico, University of Lisbon, 2020.

[21] P. Pontes. Thermographical analysis of interface heat transfer mechanisms, with high temporal resolution. Master's thesis, Instituto Superior Técnico, University of Lisbon, 2016.

[22] F. P. Incropera, D. P. DeWitt, T. L. Bergman, and A. S. Lavine. *Fundamentals of Heat and Mass Transfer*. Wiley, 6th edition, 2007.

[23] C. Y. Ho and T. K. Chu. Electrical resistivity and thermal conductivity of nice selected AISI Stainless Steels. Prepared by Center for Information and Numerical Data Analysis and Synthesis, Purdue University, 1977.

[24] M. Malý, A. S. Moita, J. Jedelsky, A. P. C. Ribeiro, and A. L. N. Moreira. Effect of nanoparticle concentration on the characteristics of nanofluid sprays for cooling applications. *Journal of Thermal Analysis and Calorimetry*, pages 1–12, 2018.